Optical Materials 175 (2026) 118034

Contents lists available at ScienceDirect

Optical Materials

journal homepage: www.elsevier.com/locate/optmat

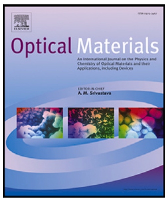

Research article

Magnesium-induced bandgap widening in NiO: An integrated theoretical–experimental study for optoelectronic applications

F. Bermúdez-Mendoza, D.J. Ramos-Ramos, G.C. Vásquez, D. Maestre, F. Domínguez-Adame, B. Méndez, A. Cremades, E. Díaz *, R. Martínez-Casado *

Departamento de Física de Materiales, Universidad Complutense, E-28040 Madrid, Spain

ARTICLE INFO

Keywords:
Density functional theory
Optoelectronics
Spectroscopy
Vacancy engineering
Oxides

ABSTRACT

This study presents a comprehensive investigation of the structural and optoelectronic properties of Mg modified NiO samples by combining experimental results and theoretical calculations. NiO thin films with variable Mg concentration have been synthesized following a low-cost and scalable route and their structural, compositional and optical properties were studied by microscopy and spectroscopy techniques. Additionally, we systematically examine NiO with varying Mg concentrations under pristine and vacancy-induced conditions by means of first principles calculations. Our findings reveal that Mg incorporation consistently widens the electronic bandgap of NiO, yielding values ranging from 4.55 eV to 4.95 eV in vacancy-free structures and from 4.02 eV to 5.02 eV in structures containing Ni vacancies. The introduction of Ni vacancies decreases the bandgap significantly by creating new states within the bandgap arising from lattice distortions and electronic disruptions. Observed bandgap trends closely adhere to Vegard's law, with calculated bowing parameters indicating significant compositional dependence in agreement with experimental results. This thorough analysis, combining experimental and theoretical approaches, highlights how precise Mg doping and vacancy engineering strategies enable targeted tuning of NiO's electronic properties, supporting their potential application in advanced optoelectronic devices.

1. Introduction

The pursuit of advanced functional materials has increasingly focused on wide and ultra-wide bandgap oxides, given their potential for high-power electronics, robust optoelectronics, and spintronic applications. Among these oxides, p-type variants are exceptionally scarce yet crucial for creating bipolar devices, transparent p–n junctions, and integrated optoelectronic systems. Nickel oxide (NiO) stands out in this regard, boasting an energy bandgap (E_g) that can range from about 3.6 eV to as high as 5.0 eV [1–4], positioning it at the boundary of the ultra-wide bandgap regime. Its intrinsic p-type conductivity, arising primarily from Ni deficiencies, underpins its utility in transparent electronics, photovoltaic systems, and energy storage applications [5,6]. Furthermore, NiO's rock salt crystal structure, combined with its antiferromagnetic (AFM) ordering at a Néel temperature near 523 K [7,8], makes it a compelling model system for investigating strong electron correlations and magnetically coupled phenomena in transition metal oxides [9]. In particular, NiO has been widely studied as a Mott insulator, where conventional band theories do not capture the correct bandgap without advanced electronic structure methods [3,10].

A core motivation for exploring NiO lies in its ability to function in the ultraviolet (UV) regime, making it attractive for photodetectors and optoelectronic devices in this spectral region [11,12]. The high thermal and chemical stability of NiO is particularly advantageous in harsh operational environments, such as those encountered in high-temperature industrial settings. Moreover, NiO's p-type character is a key ingredient for constructing heterojunctions with other wide-bandgap n-type oxides, enabling, for instance, self-powered photodetectors that exhibit high performance in the deep-UV spectral region [12]. Beyond optics, NiO's stable AFM ordering has generated significant interest in spintronic applications, where the absence of net magnetization can reduce stray magnetic fields while still permitting spin manipulation [13–15]. This versatility underlines NiO's potential to serve as a multi-functional platform, bridging optical, electronic, and magnetic domains.

Despite these attractive properties, controlling the electronic characteristics of NiO for specific device requirements remains non-trivial [16]. Doping is an especially powerful route to tailoring wide-bandgap oxides. The optical and electronic properties of a semiconductor alloy

---

* Corresponding authors.
E-mail addresses: elenadg@fis.ucm.es (E. Díaz), mariarum@ucm.es (R. Martínez-Casado).

https://doi.org/10.1016/j.optmat.2026.118034
Received 28 July 2025; Received in revised form 24 February 2026; Accepted 14 March 2026

or doped material change with the composition or doping concentration [17,18], and the experimental E_g can be predicted or estimated in several cases by the Vegard's law [19].

Knowledge of Vegard's relationship enables a precise tuning of optoelectronic properties, making it invaluable in engineering materials for targeted applications, such as NiO-based materials for UV optoelectronics and photodetectors [17]. However, synthesis methods that allow for careful control of the materials composition are required in order to corroborate these predictions.

Magnesium emerges as an exceptional dopant for NiO, since Mg^{2+} can replace Ni^{2+} maintaining charge neutrality [6,20], providing a reliable way to fine-tune NiO's bandgap and spin configuration. Indeed, doping NiO with Mg can widen the bandgap toward 5 eV, which is especially relevant for solar blind and deep UV optoelectronic applications, where a large gap is essential to minimize background absorption and enhance detector sensitivity [21]. Simultaneously, doping with Mg influences the density of Ni vacancies (V_{Ni}), which are key point defects that further modulate conductivity, carrier concentration, and local magnetic order.

The theoretical description of NiO, however, is complicated by strong on-site Coulomb interactions characteristic of Mott insulators. Conventional density functional theory (DFT) within the local density approximation (LDA) or generalized gradient approximation (GGA) often underestimates the bandgap and can misrepresent magnetic ordering [22]. More sophisticated approaches, such as hybrid functionals, which blend Hartree–Fock exchange with DFT [23–25], are frequently employed to achieve more accurate bandgaps and cohesive energies at a manageable computational cost. Even so, capturing the effects of doping and defect formation in NiO requires carefully chosen supercell models and explicit spin polarization to reflect the AFM ground state. The reliability of such simulations can be tested against advanced methods, like dynamical mean-field theory, although these typically demand substantially more computational resources [26]. Tools such as CRYSTAL23 [27], which implements Gaussian-type orbital basis sets with flexible exchange correlation functionals, are especially well suited to handle the interplay of doping, defects, and strong correlations in NiO.

In this work, we assess the structural and optical properties of Mg in NiO thin films synthesized by a low-cost and straightforward method using liquid-based precursors. To understand the electronic properties of the synthesized materials, we have carried out a systematic theoretical investigation using hybrid DFT functionals to describe Mg:NiO across a range of experimentally obtained doping concentrations. By constructing 64-atom supercells and carefully adjusting the spin channels, we isolate how Mg substitution alone primarily widens the bandgap, whereas introducing Ni vacancies triggers the formation of mid-gap states [21,28]. Our analysis of the spin density (SD), the density of states (DOS), and the band structure underscores the delicate balance between the doping level, local disorder, and electron correlation. By converging theoretical and experimental approaches, these results clarify how NiO's electronic structure evolves under the combined effects of Mg concentration and defect chemistry, providing practical insights. Overall, this study deepens our understanding of how to leverage NiO's wide bandgap and p-type character for advanced device applications.

2. Methods

2.1. Experimental methods

NiO and Mg:NiO reference samples in form of thin films have been synthesized following a liquid-based precursor method. In this case, as received Nickel Stearate powder (NiSt, Indagoo) and Magnesium Stearate powder (MgSt, Sigma Aldrich) were dispersed in 10 mL $CHCl_3$ (Sigma Aldrich) to a concentration of 5 mg/mL. Depending on the desired Mg:NiO solid solution, the nominal MgSt concentration was 0, 10, 25 and 50 wt%. The solutions were stirred on a hot plate at 65 °C for 30–60 min adding a ∼2-5 vol.% of Ethylene glycol (EG, Sigma Aldrich) as surfactant until the mixture becomes transparent and slightly greenish due to NiSt. The $\sim 1 \times 1$ cm^2 substrates (Si or silica) were previously ultrasonicated in acetone, ethanol, and deionized water, followed by nitrogen blow to remove dust particles. The coatings were fabricated by casting a 100 μL solution on the substrates with both the precursor and the substrate at 60 °C. Once the samples are completely dry, they are treated to form Mg:NiO by thermal decomposition in a tubular furnace (OBERSAL ST 112520) at atmospheric pressure. The thermal treatment consists of a heating ramp from room temperature to 350 °C at 1 °C/min rate, holding for 1 h to decompose the organic backbone from the stearic salts. An additional step increasing the temperature at 2 °C/min rate until 550 °C and holding for 2 h is required to promote the materials crystallization. Then, the samples are cooled down to room temperature naturally.

The morphological characterization of the Mg:NiO coatings was performed by scanning electron microscopy (SEM) in a Thermofisher Prisma-E SEM. The SEM is equipped with an energy dispersive X-ray spectroscopy (EDS) detector (UltraDry Silicon Drift EDS Detector) for elemental mappings and cationic quantification to determine the Mg:NiO composition (referred to as $Ni_{1-x}Mg_xO$ for simplicity). The crystalline structure of the samples was assessed by grazing incidence X-ray diffraction (GIXRD) using a Bruker D8 Advance instrument with a Cu Kα radiation (λ = 1.54158 Å) with 1° incidence angle. μ-Raman spectroscopy has been performed in a Horiba Jobin–Yvon LabRaman Hr800 confocal microscope equipped with a focused He-Cd cw-laser (ca. ∼1 μm spot size) with 325 nm wavelength output. UV-visible absorbance has been measured in samples deposited on silica with a Jasco V770 spectrophotometer equipped with an integrating sphere for diffuse reflectance spectroscopy.

2.2. Computational methods

All first-principles calculations of this study were carried out using the CRYSTAL23 code [27], which solves the Kohn–Sham equations by employing localized Gaussian-type orbital basis sets. Unlike plane-wave approaches, these localized basis sets offer direct control over the real-space resolution of the wave function, often leading to improved accuracy for systems with strong on-site Coulomb interactions, such as transition metal oxides. The Heyd–Scuseria–Ernzerhof (HSE06) screened hybrid functional was chosen for all simulations, as it provides a practical yet accurate balance between the computational demands of Hartree–Fock exchange and the need to describe electron correlation in wide-gap transition metal oxides [29]. In HSE06, a fraction of exact exchange is included in the short-range regime, reducing the well-known bandgap underestimation associated with semilocal functionals such as Perdew–Burke–Ernzerhof (PBE) functional or LDA. This partial incorporation of Hartree–Fock exchange is particularly beneficial for capturing localized d states and strong electron–electron interactions in NiO. Consequently, HSE06 is well-suited to predict the emergence of states inside the bandgap and subtle magnetic effects in systems with correlated electrons.

We modeled NiO in its rock-salt crystal structure using a $2 \times 2 \times 2$ supercell of 64 atoms (32 Ni, 32 O), adopting a lattice parameter of 4.177 Å [2]. This supercell size strikes a balance between computational tractability and the ability to capture local variations in doping and defect environments. To accurately describe Ni's strongly correlated 3d electrons, we employed a triple-zeta basis set augmented by spin-polarization functions, whereas oxygen was represented with a double-zeta basis [30]. This choice ensures sufficient flexibility for both the metal–oxygen bonding and the localized nature of Ni 3d orbitals, which is crucial for capturing AFM ordering and potential states inside the bandgap [31]. We performed geometry optimizations allowing all atomic positions to relax until the total energy converged to within 10^{-7} Hartree. Additionally, a 6×6 Monkhorst–Pack $\boldsymbol{k}$-point mesh was

Table 1
List of studied samples, nominal concentration in wt.% of MgSt in the precursor solution, and cationic concentration (cat.%) measured by EDS.

Sample	MgSt (wt.%)	Mg (cat.%)
NiO	0	0
NiO-10Mg	10	18
NiO-25Mg	25	33
NiO-50Mg	50	43

used for Brillouin zone sampling [32,33], offering a fine resolution of the electronic structure without excessively increasing computational cost. We began each simulation by assigning an AFM configuration along the (111) direction, ensuring alternating up and down spins on Ni sublattices to capture NiO's AFM-II ground state [14]. During self-consistent field iterations, we employed a 30% mixing of the new Fock matrix at each step to stabilize the convergence of the electronic density.

For direct comparison with earlier studies on NiO, we assessed the global hybrid Becke–Lee–Yang–Parr (B3LYP) functional, which mixes a fixed 20% of exact Hartree–Fock exchange as is well known for reproducing NiO's experimental bandgap. However, because B3LYP applies that exchange fraction uniformly at all distances, it lacks the dielectric screening needed to treat long-range exchange interactions realistically in solids. Therefore, we adopted the hybrid HSE06 screened as our primary functional. By retaining short-range exact exchange and replacing the long-range part with PBE exchange, HSE06 provides a more physically consistent description across the entire Mg:NiO series. Bulk MgO was modeled in a 64 atoms 2 × 2 × 2 rocksalt supercell, identical in size to NiO-based cells, ensuring consistent $\boldsymbol{k}$ point meshes, defect geometries, and relaxation protocols for all compositions.

Optical spectra were computed within the frequency-dependent coupled-perturbed Kohn–Sham (CPKS) formalism as implemented in CRYSTAL23 [27,34–36], by evaluating the dielectric tensor within the isotropic approximation $\varepsilon(\omega) = \frac{1}{3}\left(\varepsilon_{xx} + \varepsilon_{yy} + \varepsilon_{zz}\right)$, which is standard for polycrystalline and texture-free films [37]. Then the complex refractive index $\tilde{n} = n + ik$ was reconstructed from ε, and the absorption coefficient was evaluated as $\alpha(\lambda) = 4\pi k/\lambda$. For panels that compare directly with experiment we convert α to absorbance (optical density) via the Beer–Lambert relation $A(\lambda) = (\alpha d)/\ln 10$ [38]. The film thickness was set to the estimated experimental value $d = 60\,\text{nm}$, consistent with a typical ∼10–100 nm nanoparticle scale where absorption dominate the optical response of nanoparticle films [39]. Because absolute magnitudes depend on porosity, roughness, and interference, we emphasize trends and onset positions over intensities. The CPKS implementation for frequency-dependent optical response is available and robust only for semilocal functionals like PBE that are known to underestimate absolute band gaps in NiO-based oxide. To place the resulting PBE spectra on a hybrid functional quality energy scale, we aligned the results to HSE06 via a composition-dependent correction as follows. By using the calculated values $E_g^{\text{HSE06}}(x = 0) = 4.5509\,\text{eV}$ and $E_g^{\text{HSE06}}(x = 43.75\%) = 4.7318\,\text{eV}$ together with the PBE results, $E_g^{\text{PBE}}(x = 0) \approx 0.9705\,\text{eV}$ and $E_g^{\text{PBE}}(x = 43.75\%) \approx 1.0836\,\text{eV}$ [16], we define $\Delta E_g(x) = E_g^{\text{HSE06}}(x) - E_g^{\text{PBE}}(x)$. The final simulated spectra have been shifted according to ΔE_g for a direct comparison with the experimental evidence.

3. Results and discussion

3.1. Mg:NiO samples characterization

The Mg:NiO samples used as references for the theoretical study are labeled as NiO-wMg, where w represents the nominal concentration in wt.% used for the synthesis. The list of samples and the actual Mg concentration in cationic fraction (cat.%) measured by EDS is summarized in Table 1.

Figs. 1(a)–(c) show SEM images of samples with different Mg concentration deposited on Si substrates after the thermal treatment at 550 °C, as described in Section 2.1. Despite the ease of the deposition method, the coatings are extended over relatively large areas with the presence of small cracks and holes, eventually. At higher magnification, shown in Figs. S1(a)–S1(d) of the Supplementary Information, we can notice that the coatings are formed by densely packed nanoparticles with, roughly, a few tens of nm size, decreasing in size as the Mg concentration increases progressively.

By EDS we carried out a quantitative analysis of the samples' composition and, at the same time, observed their element distribution. Fig. 1(d) shows the EDS spectra from the NiO and NiO-wMg samples (w = 10, 25, 50) measured at 3 keV. In this case, low excitation energy has been used during EDS analysis to enhance the signal from the probed layer with respect to the Si substrate. An estimation of the probing depth in NiO for 3 keV electron irradiation has been calculated by CASINO software [40] resulting in 60 nm depth (Fig. S2), so, considering that the Si is still noticeable at 3 keV for all the probed samples, the coating thickness can be estimated around 60 nm in average for relatively large extensions. The secondary electron image (SE) and their corresponding Ni, O and Mg contrast maps acquired at 3 keV, shown in Fig. 1(e), confirm a homogeneous element distribution in the NiO-10Mg layer. Similar features are also observed in the EDS contrast map from the sample NiO-50Mg (Fig. S3), so there is no large phase separation even for such a high Mg content. The averaged cationic quantification resulting from the EDS spectra is in relatively good agreement with the expected Mg concentrations, being 18, 33, 43 cat.% of Mg with respect to Ni cations for the NiO-10Mg, NiO-25Mg and NiO-50Mg samples, respectively. These results are included in Table 1 and will be the values used as particular cases for the theoretical study, referred to as $\text{Ni}_{1-x}\text{Mg}_x\text{O}$ ($x = 0.18$, 0.33, 0.43) for simplicity.

The XRD patterns collected from the pure NiO and NiO-wMg samples are displayed in Fig. 2(a), including the reference diffraction peaks from the JCPDS cards No. 044-1159 and 87-0653 for NiO and MgO, respectively. The 2θ region around 53°–57° in Fig. 2(a) also shows additional contributions, marked with an asterisk, that typically emerge from the Si(100) oriented substrate in grazing incidence geometry [41]. Since both NiO and MgO crystallize in the cubic rock-salt structure, they possess a very similar XRD pattern, with peaks around 37°, 43°, 63°, 75° and 79° that correspond to diffraction peaks from the (111), (200), (220), (311) and (222) planes, respectively. The patterns from the database indicate that maxima from MgO are slightly shifted to lower angles and the relative intensity of some of them are very weak in comparison to NiO, such as the (111) and (311) peaks. No evident peak splitting is detected in the recorded XRD patterns, but all the diffraction peaks clearly broaden as the Mg concentration increases. An enlargement of the region between 35°–44.5° is shown in Fig. 2(b) where the diffraction peaks from the (111) and (200) planes can be inspected closely. Here we can see that the broadening is accompanied by a peak shifting towards lower angles, which is in good agreement with the formation of a solid solution, rather than a phase mixture.

The Raman spectra acquired with a UV laser (λ = 325 nm) is shown in Fig. 2(c). The pure NiO Raman spectrum on top of Fig. 2(c) shows a characteristic vibrational mode peaking at 579 cm^{-1} attributed to the longitudinal optical (LO) mode, and its related two-phonon scattering mode at 1137 cm^{-1} [42]. The transverse optical (TO) mode, reported around 400 cm^{-1} [42,43], is barely detected, but better resolved are the associated two-phonon processes labeled as TO+LO and 2TO peaking at 728 cm^{-1} and 900 cm^{-1}, respectively. No other significant contributions are detected (e.g., due to Ni or Mg hydroxides [43,44]) except for a narrow peak at 520 cm^{-1} associated with the Si substrate [45], that is slightly detectable in the NiO sample due to the reduced coating thickness. The NiO-wMg samples are characterized by a significant blueshift reaching 20–30 cm^{-1} for the LO and 2LO modes. It is important to note that the Si peak at 520 cm^{-1} increases the relative intensity with the Mg content while

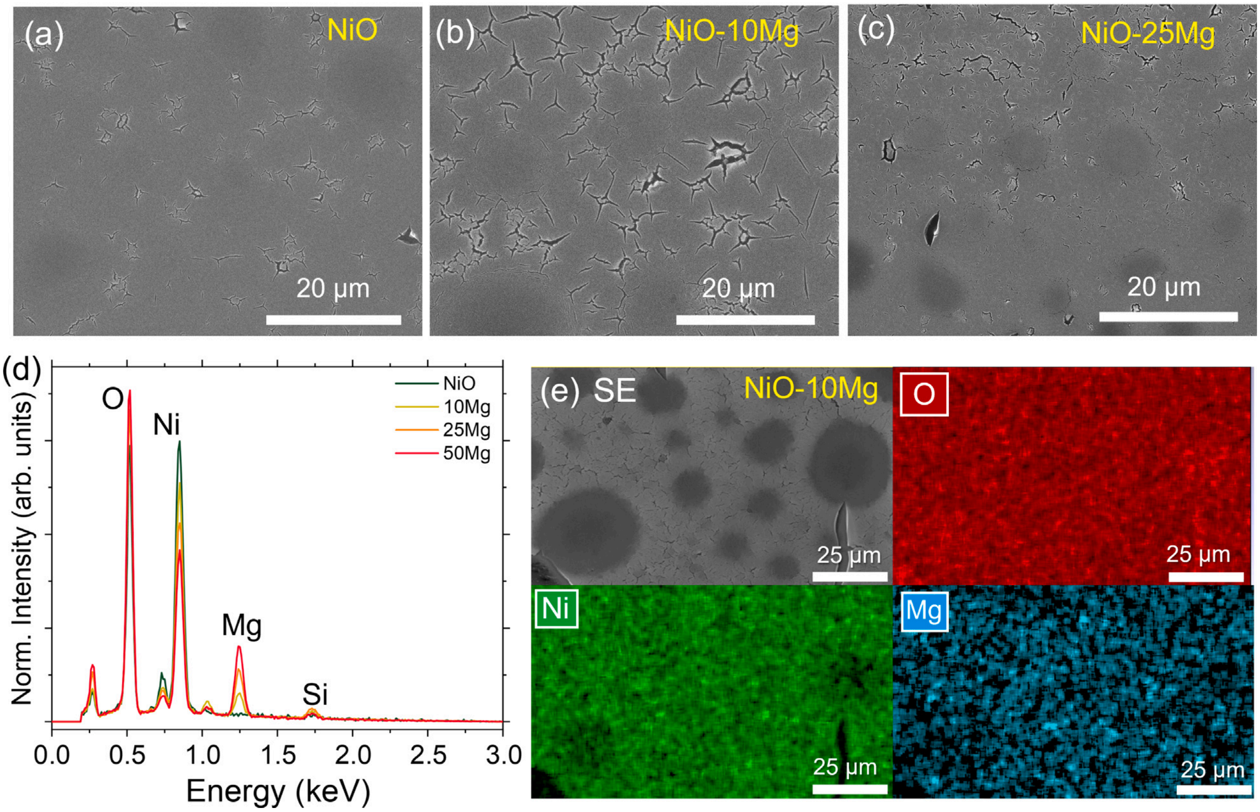

Fig. 1. SEM images from NiO and NiO-*w*Mg samples synthesized at 550 °C from solutions with mixtures of NiSt and MgSt in nominal concentrations: (a) pure NiO, (b) 10 wt% MgSt, and (c) 25 wt% MgSt. (d) EDS spectra acquired with an e-beam energy of 3 keV from NiO and NiO-*w*Mg samples. (e) SE image and its corresponding EDS contrast maps from O-K*α*, Ni-L*α* and Mg-K*α* lines obtained at 3 keV from the NiO-10Mg sample.

the characteristic signal from NiO shows a progressive broadening and quenching that is quite significant for the NiO-50Mg sample. Pure MgO is Raman inactive [44], so no additional contributions are expected in the Raman spectrum of the NiO-*w*Mg samples. However, considering that all the NiO-*w*Mg samples exhibit similar thickness, the observed peak broadening, shifting, and quenching are characteristics effects related to low dimensionality, doping and lattice disorder, while the increase of the Si related peak from the substrate is a clear indication of a change in the optical properties.

The UV-visible absorbance measured in the range between 250–650 nm for NiO and NiO-*w*Mg samples deposited on silica is shown in Fig. 3(a). The optical bandgap energy, E_g, can be determined by the Tauc's method by applying the equation $(\alpha h\nu)^n = A(h\nu - E_g)$, where α is the experimental absorption coefficient, h is the Planck constant, ν is the photon's frequency, A is a proportionality constant, and n is the exponent that can take the value 2 (or 1/2) if the nature of the optical transition is direct (or indirect), respectively. However, the experimental E_g determined by this method can be questioned since it does not always provide correct results [46]. As an alternative, the derivative approach ($\mathrm{d}\alpha/\mathrm{d}E$) does not assume the type of transition but estimates the E_g as the maximum absorption rate calculated from the experimental data [47]. Using the derivative method, the estimated E_g for NiO, NiO-10Mg, NiO-25Mg and NiO-50Mg samples are 3.76 eV, 3.85 eV, 3.97 eV and 4.11 eV, respectively. Fig. 3(b) compares the estimated E_g as a function of Mg concentration obtained from direct and indirect Tauc analyses and from the derivative method; because these are nanoparticle coatings, a weak long-wavelength scattering background persists, so E_g is extracted from the linear region at the Tauc onset (see Fig. S4 for the fit windows and extrapolations). The dotted line at 3.8 eV indicates the photon energy of the 325 nm laser used for the Raman experiments. This energy is around the NiO bandgap, thus the expected high absorption rate implies that the majority of the Raman scattering comes from shallow regions close to the surface.

It is noteworthy that our Raman results are consistent with the derivative method. In this context, the estimated E_g for pure NiO is lower than the laser energy. As the Mg concentration increases, the bandgap widens, and the films become more transparent to UV radiation, allowing the backscattered Raman signal from the Si substrate to reach the detector.

3.2. *Effects of Mg concentration and Ni vacancy on the electronic structure of NiO*

The electronic properties of NiO are known to be highly sensitive to both cation (Ni^{2+}) substitution and point defects [48], making NiO an excellent model system for exploring the interplay among doping, vacancy formation, and strong on-site Coulomb interactions [3,8]. Fig. 4 shows a representative $Ni_{1-x}Mg_xO$ AFM-Ordered supercell, where Mg occupies the same number of either spin-up and spin-down Ni sites in consecutive layers. Different Mg configurations within the supercell and their physical relevance have been investigated in Figs. S5–S6. We systematically examine how substitutional Mg defects ($\mathrm{Mg_{Ni}}$) at cationic concentrations of 18.75%, 37.50% and 43.75%, based on the samples detailed in Table 1, affects NiO's electronic structure, under both pristine conditions (no vacancies) and with a single Ni vacancy. An additional Mg value of 59.38% has been also considered in order to extend the theoretical study in the Mg:NiO regime. For completeness, Table 2 presents the formation energy associated to all considered structures.

The energy of Mg-Ni substitution formation at zero temperature is referenced to oxide reservoirs, calculated as the total energy difference referenced to the elemental bulk phases [49]:

$$E_f^{(n)}(\mathrm{Mg_{Ni}}) = E_{\mathrm{tot}}(\mathrm{Ni}_{32-n}\mathrm{Mg}_n\mathrm{O}_{32}) - E_{\mathrm{tot}}(\mathrm{Ni}_{32}\mathrm{O}_{32}) - n\left(E^{\mathrm{atom}}_{\mathrm{Mg}} - E^{\mathrm{atom}}_{\mathrm{Ni}}\right), \quad (1)$$

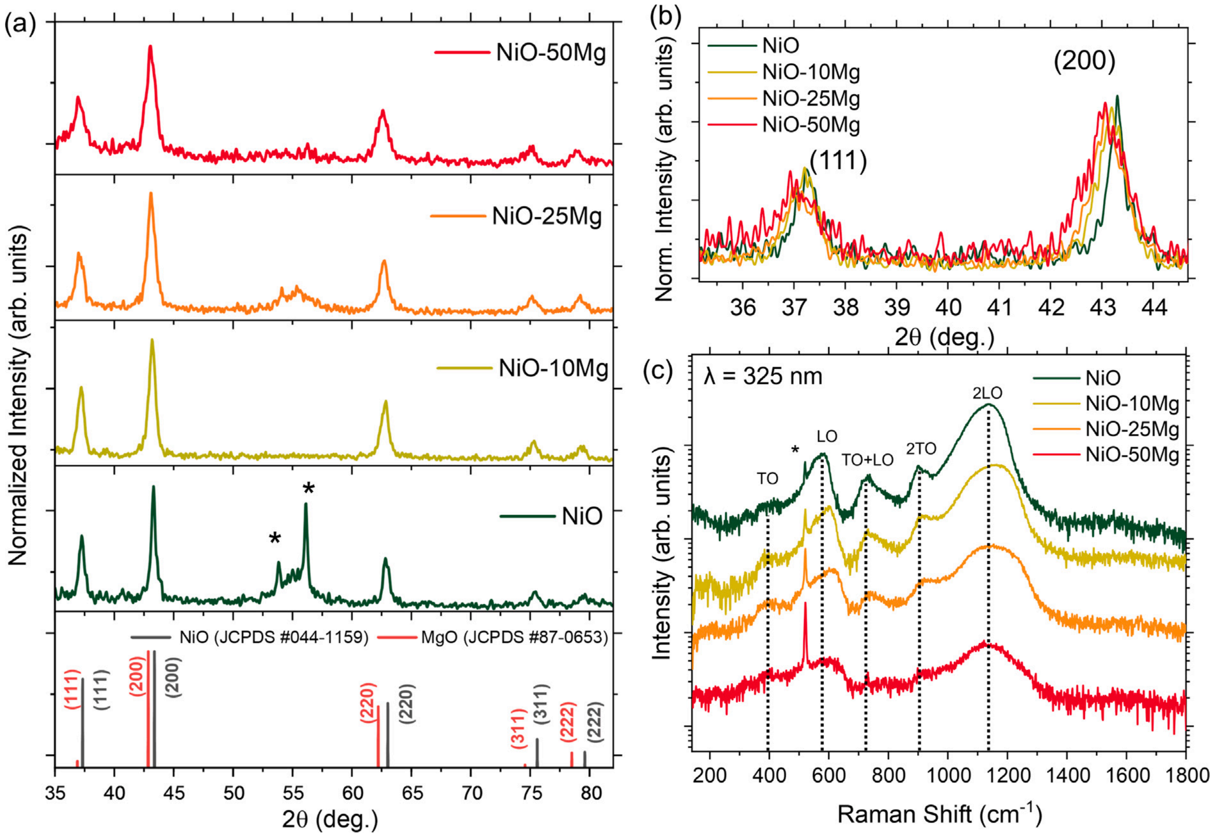

Fig. 2. (a) XRD patterns obtained in grazing incidence geometry from NiO and NiO-*w*Mg samples, and the reference peak position from JCPDS cards No. 044-1159 and 87-0653 for NiO and MgO, respectively. (b) Enlargement of the 2θ region from 35° to 44.5°. (c) Raman spectra measured with a UV laser (325 nm). The dotted lines indicate the position of the vibration modes reported for NiO.

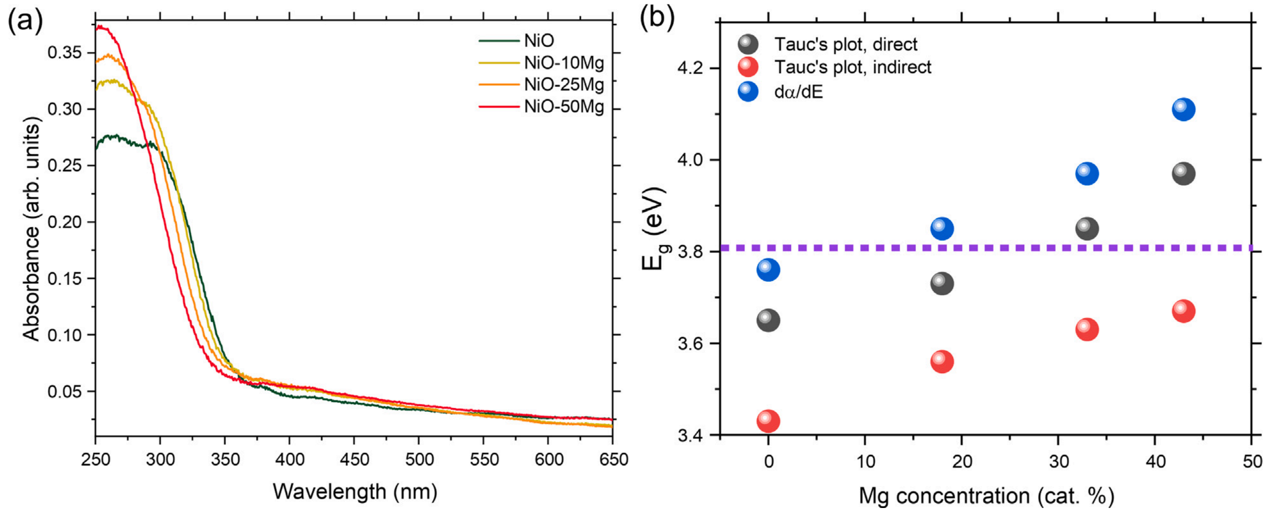

Fig. 3. (a) Experimental UV-visible absorbance data from NiO and NiO-*w*Mg samples deposited on silica. (b) Estimated optical bandgap calculated from Tauc's method for direct and indirect transitions and derivative approach. The dotted line corresponds to the photon energy used for Raman experiments.

where n is the number of substituted cations in the $2 \times 2 \times 2$ supercell ($\mathrm{Ni}_{32}\mathrm{O}_{32}$), so the Mg fraction is $x = n/32$. E_{tot} is the DFT total energy of the indicated periodic cell, and $E^{atom}_{\mathrm{Mg(Ni)}}$ is the energy per-atom (Mg or Ni) of the elemental bulk, i.e., the elemental reservoirs. The values in Table 2 decrease with Mg content, from 5.651 eV at 18.75% to 3.623 eV at 59.38%, while at $x = 0$ there is no Mg substitution and (1) results zero by construction. In order to evaluate the formation energy of Ni vacancy in a Mg-doped configuration, we use the Ni-rich Ref. [50] as follows:

$$E_f^{(n)}(V_{\mathrm{Ni}}) = E_{\mathrm{tot}}(\mathrm{Ni}_{31-n}\mathrm{Mg}_n\mathrm{O}_{32}) + E_{\mathrm{Ni}}^{\mathrm{atom}} - E_{\mathrm{tot}}(\mathrm{Ni}_{32}\mathrm{O}_{32}). \tag{2}$$

The resulting energies only vary weakly with Mg concentration (3.246–3.324 eV in Table 2). The systematic decrease of $E_f^{(n)}(\mathrm{Mg}_{\mathrm{Ni}})$ with x is consistent with the alloy energetics of NiO-MgO and reflects cooperative elastic relaxation together with the progressive dilution of Ni-O-Ni superexchange pathways as nonmagnetic Mg^{2+} replaces Ni^{2+}.

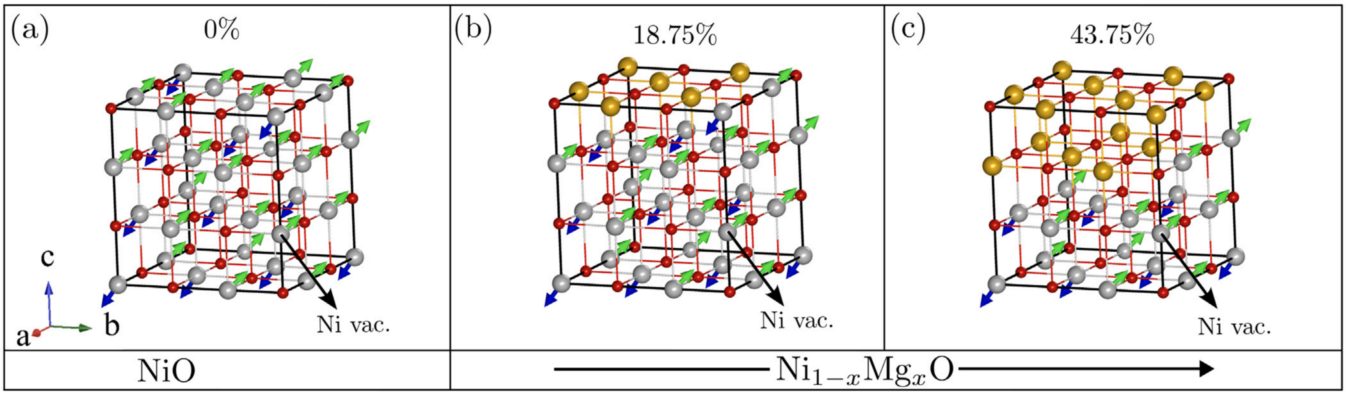

Fig. 4. Crystal structures of Mg:NiO illustrating the progressive substitution of Ni by Mg at concentrations of (a) 0% (pristine NiO), (b) 18.75%, and (c) 43.75%. The location of a representative Ni vacancy (labeled "Ni vac.") used in the calculations is indicated with a black arrow. Arrows indicate spin orientations: green for spin-up and blue for spin-down, highlighting the AFM ordering in the system.

Table 2
Formation energies for Mg substitution on Ni sites (n Mg atoms in the cell $\mathrm{Ni}_{32-n}\mathrm{Mg}_n\mathrm{O}_{32}$) and for a single Ni vacancy in the rocksalt Mg:NiO ($2 \times 2 \times 2$ AFM-Ordered supercells).

Mg (%)	n (Mg atoms)	$E_f(\mathrm{Mg_{Ni}})$ (eV)	$E_f(V_{\mathrm{Ni}})$ (eV)
0	0	–	3.276
18.75	6	5.651	3.267
37.50	12	4.712	3.324
43.75	14	4.401	3.249
59.38	19	3.623	3.246

Table 3
Equilibrium lattice constants (a_0) and corresponding bandgaps of Mg:NiO for various Mg concentrations, comparing configurations without (No vac.) and with a single Ni vacancy (With vac.). The bandgap increases upon increasing the Mg concentration, with lattice constants slightly expanding upon doping.

Mg (%)	No vac.		With vac.	
	a_0 (Å)	Bandgap (eV)	a_0 (Å)	Bandgap (eV)
0	4.169	4.551	4.166	4.02
18.75	4.177	4.553	4.168	4.15
37.50	4.185	4.682	4.179	4.69
43.75	4.188	4.732	4.180	4.80
59.38	4.195	4.956	4.188	5.02

Doping NiO with Mg leads to a systematic dilation of the lattice and a progressive increase of the bandgap, see Table 3. These trends persist regardless of whether the system is pristine or contains a single Ni vacancy. This increase arises primarily because nonmagnetic Mg^{2+} ions replace some of the Ni^{2+} ions, allowing the overall occupancy of the Ni 3d orbitals and the associated on-site Coulomb repulsion to decrease, causing the shift of the conduction band to higher energies [51,52]. Fig. 4 shows a representative Mg:NiO supercell, where various scenarios were investigated: (b)–(c) Mg substitutes Ni atoms according to an ordered filling scheme (50% spin-up, 50% spin-down).

Fig. 5 compares the spin-resolved band structures and DOS at three representative doping levels: 0%, 18.75%, and 43.75%. Spin-up (α) bands are shown in red, whereas spin-down (β) bands are shown in blue. Upper panels refer to the pristine (vacancy free) configuration and lower panels to the single-vacancy configuration. In both scenarios the main bandgap widens with increasing Mg concentration but it is the introduction of a single Ni vacancy that strongly alters the electronic structure (see lower panels of Fig. 5). The presence of the vacancy creates distinct states that reduce the apparent bandgap. Notice that in-gap states are not induced by Mg doping; rather, they clearly arise only upon the complete removal of Ni atoms. The presence of a single Ni vacancy, whether in the spin-up or spin-down sublattice, depletes the electron density near the vacancy site and triggers subtle rearrangements in the magnetic moments of neighboring Ni ions. This process is tied to the emergence of Ni^{3+} states, which promote localized hole formation and significantly alter NiO's overall electronic and magnetic properties [53,54]. This behavior aligns with previous first principles studies showing that missing cations can modify local superexchange interactions in NiO [55,56]. Consequently, doping and defect formation operate hand in hand, providing a finer degree of control over NiO's conduction mechanisms and AFM structure.

In the presence of a Ni vacancy, the electronic response is controlled by in-gap states that arise close to the top of the valence band. However, the introduction of Mg leads to the vanishing of these states that become part of the valence band improving overall transport properties, see lower panels of Figs. 5(a)–(c). Our hybrid-DFT values represent fundamental gaps for bulk-like periodic supercells at zero temperature, whereas the measurements probe room-temperature optical onsets in nanocrystalline $\mathrm{Ni}_{1-x}\mathrm{Mg}_x\mathrm{O}$ coatings. Several effects systematically depress the experimental onset relative to the fundamental gap, including finite-temperature electron–phonon coupling, excitonic binding, and defect states associated with surface and grain boundaries. Quantum confinement is negligible at the observed particle sizes, so there is no compensating blue shift. The inclusion of a single Ni vacancy in the calculations captures part of this nanostructure and defect-driven physics, thereby narrowing the discrepancy between theory and experiment [16].

Last, in order to differentiate chemical from spin effects, we repeated the calculations at 43.75% Mg in a spin-up selective substitution that we refer to as *spin control*, where Mg occupies a single AFM sublattice. This configuration biases the residual Ni moments toward the same sign (spin-down; Fig. S5(c)), i.e., an almost perfect ferromagnetic (FM) spin texture. The vacancy-free supercell exhibits a band gap of 4.66 eV, while the inclusion of a neutral Ni vacancy generates spin-polarized in-gap states, which reduces the apparent gap to 4.47 eV (Table I in Supplemental Information). The spin control configuration leaves the Mg-substitution energetics essentially unchanged, $E_f(\mathrm{Mg_{Ni}}) = 4.413\,\mathrm{eV}$ (AFM-ordered: $4.401\,\mathrm{eV}$, $\Delta < 0.3\%$), but lowers the neutral Ni-vacancy formation energy by $\Delta \sim 11\%$, from $3.249\,\mathrm{eV}$ (AFM-ordered) to $2.891\,\mathrm{eV}$ (spin-control). Experimental evidence on magnetic properties of Mg:NiO solutions doped with low concentrations of Mg have revealed weak FM-like loops associated to uncompensated surface spins and oxygen vacancies, that coexist with an AFM background [21,28,57].

Fig. 6 shows the spin density (SD) distribution for NiO at varying Mg concentrations (0%, 18.75%, and 43.75%) under pristine conditions (top row) and with a single Ni vacancy (bottom row). SD maps show regions of spin-up (red) and spin-down (blue) states in arbitrary units. At zero doping (0%), the characteristic AFM order of pristine NiO

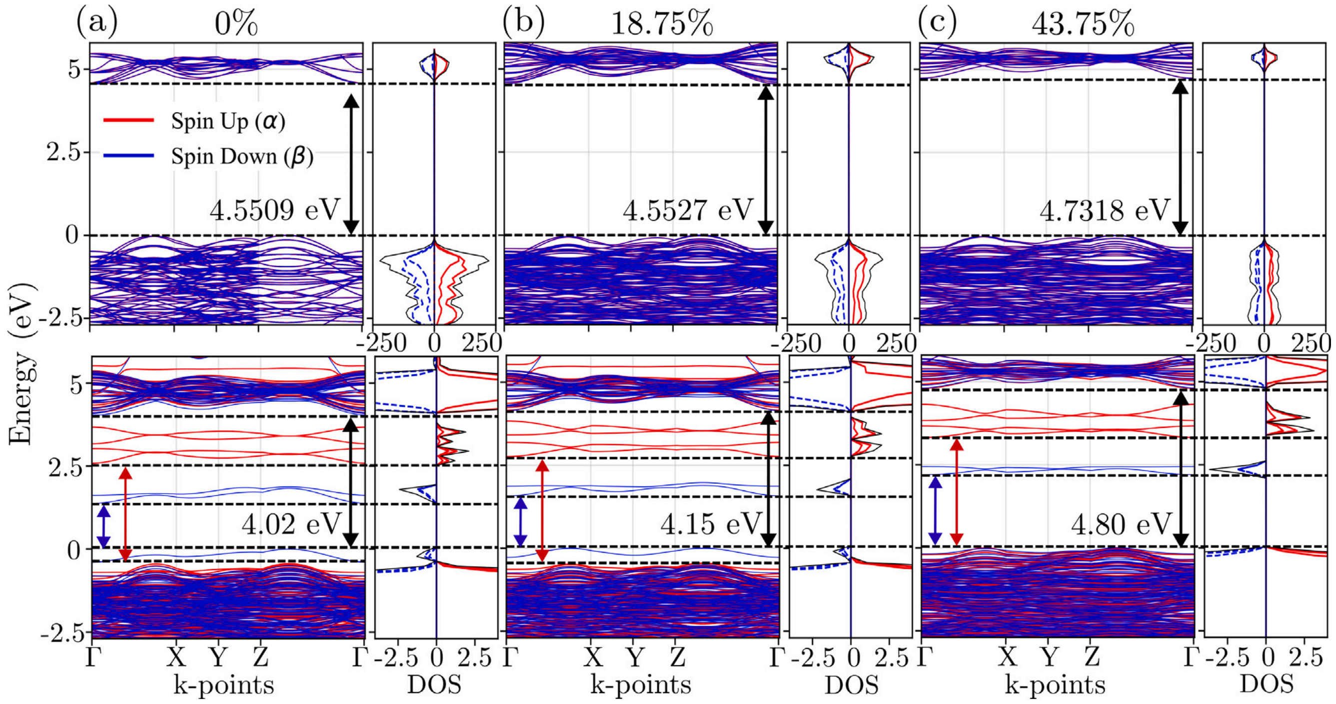

Fig. 5. Electronic band structures and DOS (in arbitrary units) of NiO for Mg concentrations of (a) 0%, (b) 18.75%, and (c) 43.75%. Spin-up (α) states are indicated by red lines, and spin-down (β) states by blue lines. The DOS on the right of each band structure highlights the electronic distribution. Upper panels (without vacancy) show a broader range of states to illustrate overall trends clearly, whereas lower panels (with vacancy) provide a magnified view to reveal states within the bandgap, which also manifest clearly in the DOS. Arrows and numerical values indicate the bandgap, which increases with higher Mg concentration.

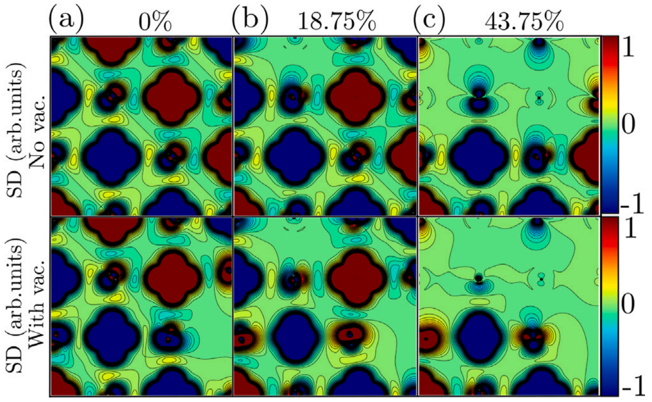

Fig. 6. Spin density (SD) distributions across the (100) plane for Mg:NiO at Mg concentrations of (a) 0%, (b) 18.75%, and (c) 43.75%, comparing scenarios without vacancies (top row) and with a single Ni vacancy (bottom row). Spin-up and spin-down states are represented in red and blue colors, respectively, in arbitrary units. The progressive increase in Mg concentration and the introduction of a Ni vacancy clearly modify the local SD patterns, reflecting their impact on the electronic and magnetic structure of NiO.

is clearly observed, with neighboring Ni sites carrying antiparallel magnetic moments [14]. When replacing magnetic Ni ions with non-magnetic Mg ions, the local spin distributions become progressively altered, indicating a reduction in magnetic interactions due to the disruption of Ni–O–Ni linkages [58], see lower panels of Fig. 6.

The introduction of a Ni vacancy induces a strong local perturbation in the electronic and magnetic structure of NiO. The removal of a Ni^{2+} ion leads to charge redistribution and spin polarization of the surrounding Ni and O atoms, giving rise to defect states with mixed Ni-3d and O-2p character within the bandgap. These states are associated with a local imbalance of magnetic moments, as evidenced by the spin-resolved band structures and spin-density maps. In contrast, Mg substitution does not generate magnetic moments by itself, as Mg^{2+} is nonmagnetic. Instead, increasing Mg concentration progressively dilutes the Ni–O–Ni magnetic network, redistributing the vacancy-induced magnetic polarization over a larger spatial region. As the Mg concentration increases, these localized spin perturbations gradually delocalize, owing to the gradual replacement of magnetic Ni^{2+} ions by nonmagnetic Mg^{2+} ions.

To account for the magnetic structure induced by $V_{\rm Ni}$ or the Mg doping, we evaluate the local atomic spin moment $m_i = N_i^\alpha - N_i^\beta$ on each atom i where N_i^σ ($\sigma = \alpha, \beta$) is the spin-resolved atomic population obtained from the spin density matrix as implemented for periodic systems in [27]. From the set $\{m_i\}$ we report three scalar descriptors: the average absolute Ni moment, $m_{\rm Ni}^{\rm av} = \frac{1}{N_{\rm Ni}} \sum_{i\in{\rm Ni}} |m_i|$, the minimum Ni moment, $m_{\rm Ni}^{\rm min} = \min_{i\in{\rm Ni}} |m_i|$, and the maximum oxygen moment $m_{\rm O}^{\rm max} = \max_{i\in{\rm O}} |m_i|$. The latter typically corresponding to a Ni(O) atom adjacent to $V_{\rm Ni}$. In pristine NiO we obtain $m_{\rm Ni}^{\rm av} \simeq 1.696\ \mu_{\rm B}$ together with a negligible oxygen polarization, consistent with the magnetic structure AFM-II [14,59]. The introduction of a single vacancy $V_{\rm Ni}$ produces a strong local spin rearrangement, so that $m_{\rm Ni}^{\rm av}$ decreases to $1.631\ \mu_{\rm B}$, and the most perturbed neighboring Ni leads to $m_{\rm Ni}^{\rm min} \simeq 1.405\ \mu_{\rm B}$. Additionally a sizeable ligand polarization emerges at a neighboring O such that $m_{\rm O}^{\rm max} \simeq 0.134\ \mu_{\rm B}$. This behavior is consistent with a vacancy-induced hole with mixed Ni-3d and O-2p character in this material [3,9,60–62]. On the other hand, when Ni atoms are substituted by Mg, although $m_{\rm Ni}^{\rm av}$ stays nearly constant at $\sim 1.67\ \mu_{\rm B}$, such spin density is progressively transferred toward the oxygen sublattice. Indeed $m_{\rm O}^{\rm max}$ increases from $0.195\ \mu_{\rm B}$ at 18.75% Mg to $0.362\ \mu_{\rm B}$ at 43.75% Mg while Mg remains essentially nonmagnetic $m_{\rm Mg}^{\rm max} \lesssim 0.015\ \mu_{\rm B}$. This quantitative trend complements the SD maps in Fig. 6 and shows that Mg does not create magnetism by itself, but reshapes the vacancy-induced polarization cloud by diluting the magnetic Ni-O-Ni network with nonmagnetic Mg^{2+} ions as mentioned before [58].

This magnetic redistribution is closely correlated with the evolution of vacancy-induced electronic levels that govern their electronic

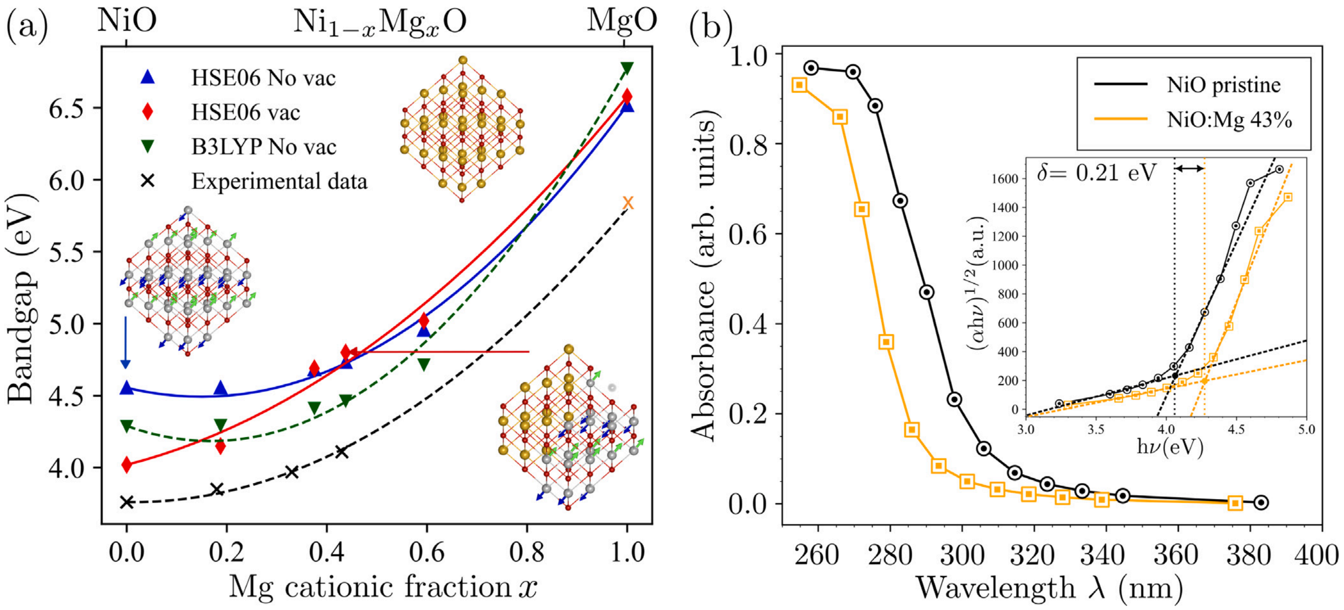

Fig. 7. (a) Calculated bandgap of rocksalt $Ni_{1-x}Mg_xO$ as a function of Mg fraction x. Blue upright triangles are HSE06 results for stoichiometric supercell (no vacancies); red diamonds are HSE06 results with one Ni vacancy; green downward triangles are B3LYP results for an stoichiometric supercell; black curve represent experimental values from Fig. 3 and the orange cross is a value taken from the literature [63–65]. All curves are quadratic Vegard type fits obtained from Eq. (3). The insets display 2 × 2 × 2 supercells in the crystalline plane (111) of pure NiO (left), pure MgO (center), and a $x = 0.43$ alloy containing a single Ni vacancy (right), with Ni, Mg, and O ions depicted in gray, gold, and red, respectively, and the vacancy site indicated by a semitransparent sphere. (b) Calculated absorbance (arb. units) of pristine NiO and $Ni_{0.57}Mg_{0.43}O$. The corresponding inset shows the corresponding indirect Tauc representation $(\alpha h\nu)^{1/2}$ as a function of photon energy $h\nu$. The intersection of linear fits to the baseline and absorption edge yields an optical bandgap widening of $\delta = 0.21$ eV for $x = 0.43$, in close agreement with the experimentally determined indirect optical bandgap widening for $\delta = 0.19$ eV in Fig. 3(b).

response. In supercells containing a Ni vacancy (V_{Ni}), the spin-polarized states appearing within the apparent bandgap originate from defect levels localized mainly on the first coordination shell surrounding the vacancy. In particular, the acceptor-like band states, localized on oxygen atoms and lying close to the valence-band maximum, are the most strongly affected by Mg incorporation. As the Mg concentration increases, this particular vacancy-related band progressively hybridizes with the valence band, as observed in the lower panels of Fig. 5.

This magnetic and electronic redistribution plays a key role in regulating the optical response of the material. Ni-vacancy-induced states enhance sub-bandgap absorption and effectively narrow the optical bandgap. As a consequence, the absorption onset shifts toward higher photon energies, leading to a widening of the optical bandgap. This mechanism consistently explains the experimentally observed blue shift in the UV–visible spectra and the trends obtained from hybrid-DFT calculations. This interpretation is consistent with the widening of the bandgap series reported in Table 3 when the V_{Ni} is present, as well as with the improved electrical performance in Mg-doped NiO [6,61].

As mentioned in the Introduction, variations in the bandgap of a solid solution can be described by the well-known Vegard's law [17,18]. Accordingly, for $Ni_{1-x}Mg_xO$ systems, the resulting bandgap $E_{Ni_{1-x}Mg_xO}(x)$ at a given Mg concentration x can be expressed as follows

$$E_{Ni_{1-x}Mg_xO}(x) = (1-x)\,E_{NiO} + x\,E_{MgO} - bx(1-x)\ . \tag{3}$$

Here, the bowing parameter b quantifies how much the alloy's bandgap curve bends away from the straight-line interpolation between its limiting pure semiconductors. Let us analyze the evolution of the simulated bandgap of the alloy as a function of the Mg cationic fraction shown in Fig. 7(a), where experimental values from Fig. 3 have been also included. Here red symbols account for cases where a single Ni vacancy is present, while blue ones do not consider it. Although the simulated values slightly overestimate the experimental ones the qualitative behavior is perfectly reproduced by our calculations. We attribute part of this deviation to the nanoscale character of the samples: finite-size and surface-defect effects renormalize the optical bandgap, a trend our calculations replicate when a Ni vacancy is included. [63–65]. The data points correspond to the computed bandgap values at different Mg fractions by considering the range between pure NiO ($x = 0$) to pure MgO ($x = 1$). In the absence of a Ni vacancy, the bandgap initially shows only a modest increase at lower Mg doping levels (from approximately 4.55 eV at $x = 0$ to 4.95 eV at $x = 0.5938$), followed by a more pronounced rise as the system approaches the composition of pure MgO (around 6.58 eV). This nonlinear behavior is characteristic of alloyed systems and it can be understood in terms of Vegard's law.

The observed curvature in the blue data suggests deviation from an ideal linear interpolation due to local structural relaxations, electronic effects, and changes in crystal field splitting as Ni ions are progressively substituted by Mg [17–19,66]. The introduction of single Ni vacancy significantly reduces the apparent bandgap as already discussed. Still by increasing the Mg concentration in presence of the Ni vacancy the main bandgap steadily widens as shown by the red symbols. The presence of vacancies introduces defect-induced states within the bandgap even at lower Mg doping levels, thereby causing the initial narrowing of the gap (4.02 eV for $x = 0$). However, the increasing substitution of magnetic Ni ions by nonmagnetic Mg ions gradually widens the bandgap towards the MgO limit [67].

In order to quantitatively analyze the trends observed in Fig. 7(a), the calculated data points were fitted using Eq. (3). The resulting bowing parameters were found to be 2.80 eV for the scenario without vacancies [68], and 1.68 eV with vacancies. The larger bowing parameter observed in the vacancy-free case indicates a more significant deviation from the linear trend, suggesting stronger compositional and electronic interactions between Ni and Mg ions, namely, non-linear interactions produced by composition-dependent orbital mixing (Ni 3d–O 2p versus Mg 3s/3p), local strain from the Ni–O/Mg–O bond length mismatch, and the associated electrostatic and exchange–correlation effects. In contrast, the smaller bowing parameter obtained for the case in the presence of a Ni vacancy case reflects weaker nonlinear interactions due to defect-induced states, highlighting the vacancy's role in altering local electronic environments and moderating compositional effects. The experimental bowing parameter found is 2.09 eV, which lies between our theoretical predictions. This intermediate value implies that real samples may contain a mixture of pristine and defect-containing regions, thus supporting the relevance of the theoretical model in capturing the electronic response of Mg:NiO.

In Fig. 7(a) we can observe the deviation of the calculated bandgap of two hybrid functionals HSE06 and B3LYP [17] in the configurations where no Ni-vacancy has been introduced. For Ni-rich alloys both approaches track each other reasonably well, but as the Mg content grows, the curves differentiate from each other. B3LYP climbs too steeply because its unscreened exchange overestimates the wide, highly ionic gap of pure MgO, whereas HSE06 with its built in long-range screening anchors the MgO endpoint close to experiment. Thus, B3LYP overestimates the bowing parameter which results in 3.74 eV. In short, capturing the long-range interactions that dominate in MgO is important for a reliable bowing analysis, and the screened nature of HSE06 provides that correction [69].

Fig. 7(b) compares the calculated absorbance spectra for $Ni_{1-x}Mg_xO$ at $x = 0$ and $x = 0.43$, showing an absorption onset at higher photon energies for the Mg-alloyed composition, consistent with the experimental absorbance trend observed in Fig. 3(a). To quantify this effect, the optical bandgap is determined from indirect Tauc plot analysis. The experimental indirect Tauc plots shown in Fig. 3(b) yield an optical bandgap widening of $\delta = 0.19$ eV, while the CPKS simulated optical response gives a comparable increase of $\delta = 0.21$ eV from the intersection between linear fits to the sub-bandgap baseline and the absorption edge in the indirect Tauc representation $(\alpha h\nu)^{1/2}$ (inset of Fig. 7(b)). The close agreement in δ confirms that the shift in the absorbance spectra of Fig. 7(b) is consistent with a Mg-induced widening of the optical bandgap in NiO.

4. Conclusions

This study systematically explores the effects of Mg defects and Ni vacancies on the optoelectronic and structural properties of NiO combining experimental and hybrid-DFT methods. NiO thin films with thickness around 60 nm and variable Mg concentration were synthesized using a low-cost and easily scalable method based on liquid precursors and thermal decomposition. Our findings reveal that Mg substitution in NiO leads to a consistent expansion of the atomic lattice and a progressive widening of the bandgap, both in pristine systems and those containing a single Ni vacancy. Trends of the calculated bandgap are in good agreement with the experimental values. The replacement of magnetic Ni^{2+} ions by nonmagnetic Mg^{2+} reduces the occupancy of Ni 3d orbitals, diminishing on-site Coulomb interactions and shifting the conduction band to higher energies. This mechanism explains the observed increase of the bandgap, reaching up to 5.02 eV at 59.38% Mg content.

Ni vacancies significantly alters the electronic structure and reduce the bandgap. However, higher concentrations of Mg widens the underlying bandgap. SD analyses further demonstrate how Mg disrupts the AFM order of NiO, progressively weakening magnetic interactions as nonmagnetic ions replace Ni atoms. The presence of a Ni vacancy amplifies local spin perturbations, but these effects gradually disappear with higher Mg content, reinforcing the role of Mg in stabilizing the electronic and magnetic properties favorable for conductivity.

The evolution of the bandgap with Mg content follows a nonlinear Vegard's behavior, with bowing parameters highlighting the complex interplay between composition, defects, and electronic structure. The DFT functional HSE06 provides accurate predictions, particularly at the Mg-rich end due to its effective long-range screening, leading to bowing parameters that closely align with experimental observations. The bowing parameter derived from experimental data reflects a crystallographic landscape that is neither fully pristine nor heavily defective, but rather the heterogeneous state characteristic of oxide nanoparticles. CRYSTAL23 based absorption calculations reproduce the experimental tendency that Mg substitution in NiO widens the optical bandgap matching the experiments. Overall, this work underscores the critical role of controlled doping and defect engineering in tuning the electronic properties of NiO-based materials, offering valuable insights for the design of advanced functional oxides in electronic and optoelectronic devices.

CRediT authorship contribution statement

F. Bermúdez-Mendoza: Writing – original draft, Software, Methodology, Investigation, Formal analysis, Data curation, Conceptualization. **D.J. Ramos-Ramos:** Writing – original draft, Methodology, Investigation, Data curation, Conceptualization. **G.C. Vásquez:** Writing – review & editing, Writing – original draft, Methodology, Investigation, Data curation, Conceptualization. **D. Maestre:** Writing – review & editing, Writing – original draft, Validation, Investigation, Conceptualization. **F. Domínguez-Adame:** Writing – review & editing, Validation, Formal analysis, Conceptualization. **B. Méndez:** Writing – review & editing, Validation, Methodology, Investigation, Funding acquisition, Data curation, Conceptualization. **E. Díaz:** Writing – review & editing, Writing – original draft, Supervision, Investigation, Conceptualization. **R. Martínez-Casado:** Writing – review & editing, Validation, Supervision, Software, Methodology, Investigation, Formal analysis, Conceptualization.

Declaration of competing interest

The authors declare that they have no known competing financial interests or personal relationships that could have appeared to influence the work reported in this paper.

Acknowledgments

This work was supported by the “(MAD2D-CM)-UCM” project funded by Comunidad de Madrid, Spain, by the Recovery, Transformation and Resilience Plan, and European Union NextGenerationEU/PRTR. The authors also acknowledge funding from Agencia Estatal de Investigación of Spain (MCIN/AEI/10.13039/501100011033) through Grants PCI2023-143388, PID2021-122562-NB-I00 and PID2022-136285NB-C31.

Appendix A. Supplementary data

Supplementary material related to this article can be found online at https://doi.org/10.1016/j.optmat.2026.118034.

Data availability

No data was used for the research described in the article.

References

[1] K. Baraik, R. Roychowdhury, A. Bose, C. Mukherjee, T. Ganguli, S.D. Singh, Investigation of crystalline and band alignment properties of NiO/GaN and $NiO_{0.5}Co_{0.50}$/GaN heterojunctions using synchrotron radiation based techniques, Phys. Scr. 99 (6) (2024) 065951.

[2] F. Fiévet, P. Germi, F. de Bergevin, M. Figlarz, Lattice parameter, microstrains and non-stoichiometry in NiO. Comparison between mosaic microcrystals and quasi-perfect single microcrystals, J. Appl. Crystallogr. 12 (4) (1979) 387–394.

[3] G.A. Sawatzky, J.W. Allen, Magnitude and origin of the band gap in NiO, Phys. Rev. Lett. 53 (1984) 2339–2342.

[4] A.B. Kunz, Electronic structure of NiO, J. Phys. C: Solid State Phys. 14 (16) (1981) L455.

[5] E.L. Ratcliff, J. Meyer, K.X. Steirer, A. Garcia, J.J. Berry, D.S. Ginley, D.C. Olson, A. Kahn, N.R. Armstrong, Evidence for near-surface NiOOH species in solution-processed NiO_x selective interlayer materials: Impact on energetics and the performance of polymer bulk heterojunction photovoltaics, Chem. Mater. 23 (22) (2011) 4988–5000.

[6] L. Huang, Y. Wang, X. Zhu, X. Zhao, G. Li, L. Li, W. Sun, Mg-doped nickel oxide as efficient hole-transport layer for perovskite photodetectors, J. Phys. Chem. C 125 (29) (2021) 16066–16074.

[7] N. Rinaldi-Montes, P. Gorria, D. Martínez-Blanco, A.B. Fuertes, I. Puente-Orench, L. Olivi, J.A. Blanco, Size effects on the Néel temperature of antiferromagnetic NiO nanoparticles, AIP Adv. 6 (5) (2016) 056104.

[8] H. Hopoğlu, D. Kaya, M.M. Maslov, S. Kaya, İ. Demir, İ. Altuntaş, F. Ungan, M. Akyol, A. Ekicibil, E. Şenadım Tüzemen, Investigating the optical, electronic, magnetic properties and DFT of NiO films prepared using RF sputtering with various argon pressures, Phys. B: Condens. Matter. 661 (2023) 414937.

[9] J. Zaanen, G.A. Sawatzky, J.W. Allen, Band gaps and electronic structure of transition-metal compounds, Phys. Rev. Lett. 55 (1985) 418–421.

[10] M.J. DelloStritto, A.D. Kaplan, J.P. Perdew, M.L. Klein, Predicting the properties of NiO with density functional theory: Impact of exchange and correlation approximations and validation of the r2SCAN functional, APL Mater. 11 (6) (2023) 060702.

[11] V.N. Hegde, Structural, dielectric, and optoelectronic properties of green synthesized NiO nanoparticles, Mater. Chem. Phys. 333 (2025) 130319.

[12] X. Tang, Y. Lu, R. Lin, C.-H. Liao, Y. Zhao, K.-H. Li, N. Xiao, H. Cao, W. Babatain, X. Li, Flexible self-powered DUV photodetectors with high responsivity utilizing Ga_2O_3/NiO heterostructure on buffered Hastelloy substrates, App. Phys. Lett. 122 (12) (2023) 121101.

[13] S.A. Makhlouf, H. Al-Attar, R. Kodama, Particle size and temperature dependence of exchange bias in NiO nanoparticles, Solid State Commun. 145 (1) (2008) 1–4.

[14] Y.Y. Kyuhyun Lee, S. Han, Identification of ground-state spin ordering in antiferromagnetic transition metal oxides using the Ising model and a genetic algorithm, Sci. Technol. Adv. Mater. 18 (1) (2017) 246–252.

[15] L. Li, Y. Kanai, Antiferromagnetic structures and electronic energy levels at reconstructed NiO(111) surfaces: A DFT + U study, Phys. Rev. B 91 (2015) 235304.

[16] F. Bermúdez-Mendoza, D.J. Ramos-Ramos, M. Taeño, G.C. Vásquez, D. Maestre, F. Domínguez-Adame, B. Méndez, R. Martínez-Casado, E. Díaz, Impact of Ni and O vacancies on the electronic properties of NiO: A DFT-based study for optoelectronic applications, APL Mater. 13 (9) (2025) 091115.

[17] C.A. Niedermeier, M. Råsander, S. Rhode, V. Kachkanov, B. Zou, N. Alford, M.A. Moram, Band gap bowing in $Ni_xMg_{1-x}O$, Sci. Rep. 6 (1) (2016) 31230.

[18] D. Stroud, Band gaps of semiconductor alloys, Phys. Rev. B 5 (1972) 3366–3368.

[19] L. Vegard, Die konstitution der mischkristalle und die raumfüllung der atome, Z. Phys. 5 (1) (1921) 17–26.

[20] S. Ghosh, N. Mammen, S. Narasimhan, Descriptor for the efficacy of aliovalent doping of oxides and its application for the charging of supported Au clusters, J. Phys. Chem. C 123 (32) (2019) 19794–19805.

[21] B. Govindarajan, R. Palanimuthu, K.M. Manikandan, Influence of Mg doping in magnetic properties of NiO nanoparticles and its electrical applications, J. Mater. Sci.: Mater. Electron. 30 (7) (2019) 6519–6527.

[22] J. Gebhardt, C. Elsässer, DFT with corrections for an efficient and accurate description of strong electron correlations in NiO, J. Condens. Matter Phys. 35 (20) (2023) 205901.

[23] A.D. Becke, Density-functional thermochemistry. III. The role of exact exchange, J. Chem. Phys. 98 (7) (1993) 5648–5652.

[24] P.J. Stephens, F.J. Devlin, C.F. Chabalowski, M.J. Frisch, Ab initio calculation of vibrational absorption and circular dichroism spectra using density functional force fields, J. Phys. Chem. C 98 (45) (1994) 11623–11627.

[25] M. Lorenz, M.S.R. Rao, T. Venkatesan, E. Fortunato, P. Barquinha, R. Branquinho, D. Salgueiro, R. Martins, E. Carlos, A. Liu, F.K. Shan, M. Grundmann, H. Boschker, J. Mukherjee, M. Priyadarshini, N. DasGupta, D.J. Rogers, F.H. Teherani, E.V. Sandana, P. Bove, K. Rietwyk, A. Zaban, A. Veziridis, A. Weidenkaff, M. Muralidhar, M. Murakami, S. Abel, J. Fompeyrine, J. Zuniga-Perez, R. Ramesh, N.A. Spaldin, S. Ostanin, V. Borisov, I. Mertig, V. Lazenka, G. Srinivasan, W. Prellier, M. Uchida, M. Kawasaki, R. Pentcheva, P. Gegenwart, F.M. Granozio, J. Fontcuberta, N. Pryds, The 2016 oxide electronic materials and oxide interfaces roadmap, J. Phys. D: Appl. Phys. 49 (43) (2016) 433001.

[26] S. Mandal, K. Haule, K.M. Rabe, D. Vanderbilt, Systematic beyond-DFT study of binary transition metal oxides, Npj Comput. Mater. 5 (1) (2019) 115.

[27] A. Erba, J.K. Desmarais, S. Casassa, B. Civalleri, L. Donà, I.J. Bush, B. Searle, L. Maschio, L. Edith-Daga, A. Cossard, C. Ribaldone, E. Ascrizzi, N.L. Marana, J.-P. Flament, B. Kirtman, CRYSTAL23: A program for computational solid state physics and chemistry, J. Chem. Theory Comput. 19 (20) (2023) 6891–6932.

[28] U.K. Panigrahi, V. Sathe, P.D. Babu, A. Mitra, P. Mallick, Effect of Mg doping on the improvement of photoluminescence and magnetic properties of NiO nanoparticles, Nano Express 1 (2) (2020) 020009.

[29] J. Heyd, G.E. Scuseria, M. Ernzerhof, Hybrid functionals based on a screened Coulomb potential, J. Chem. Phys. 118 (18) (2003) 8207–8215.

[30] D. Vilela Oliveira, J. Laun, M.F. Peintinger, T. Bredow, BSSE-correction scheme for consistent gaussian basis sets of double- and triple-zeta valence with polarization quality for solid-state calculations, J. Comput. Chem. 40 (27) (2019) 2364–2376.

[31] T. Bredow, A.R. Gerson, Effect of exchange and correlation on bulk properties of MgO, NiO, and CoO, Phys. Rev. B 61 (2000) 5194–5201.

[32] H.J. Monkhorst, J.D. Pack, Special points for Brillouin-zone integrations, Phys. Rev. B 13 (1976) 5188–5192.

[33] J.D. Pack, H.J. Monkhorst, "Special points for Brillouin-zone integrations"—a reply, Phys. Rev. B 16 (1977) 1748–1749.

[34] L. Maschio, M. Rérat, B. Kirtman, R. Dovesi, Calculation of the dynamic first electronic hyperpolarizability $\beta(-\omega_\sigma;\omega_1,\omega_2)$ of periodic systems: Theory, validation, and application to multi-layer MoS_2, J. Chem. Phys. 143 (2015) 244102.

[35] M. Ferrero, M. Rérat, R. Orlando, R. Dovesi, The calculation of static polarizabilities of 1–3D periodic compounds. the implementation in the CRYSTAL code, J. Comput. Chem. 29 (9) (2008) 1450–1459.

[36] M. Ferrero, M. Rérat, R. Orlando, R. Dovesi, I.J. Bush, Coupled perturbed Kohn–Sham calculation of static polarizabilities of periodic compounds, J. Phys.: Conf. Ser. 117 (2008) 012016.

[37] M. Gajdoš, K. Hummer, G. Kresse, J. Furthmüller, F. Bechstedt, Linear optical properties in the projector-augmented wave methodology, Phys. Rev. B 73 (4) (2006) 045112.

[38] P. Atkins, J. de Paula, J. Keeler, Atkins' Physical Chemistry, Eleventh ed., Oxford University Press, Oxford, 2018, Beer–Lambert relation in the spectroscopy chapter.

[39] C.F. Bohren, D.R. Huffman, Absorption and Scattering of Light by Small Particles, Wiley, New York, 1983, Canonical reference on optical response of ∼10–100 nm particles, including sizes around 60 nm.

[40] D. Drouin, CASINO a powerful simulation tool for cathodoluminescence applications, Microsc. Microanal. 12 (S02) (2006) 1512.

[41] K.L. Ganapathi, N. Bhat, S. Mohan, Optimization and integration of ultrathin e-beam grown HfO_2 gate dielectrics in MoS_2 transistors, J. Phys. D: Appl. Phys. 54 (44) (2021) 445302.

[42] D.J. Ramos-Ramos, G.C. Vásquez, D. Maestre, Micro- and nanocrystalline NiO synthesized by joule heating and thermal oxidation methods: A comparative study, Cryst. Growth Des 25 (4) (2025) 1101–1110.

[43] J. Gallenberger, H. Moreno Fernández, A. Alkemper, M. Li, C. Tian, B. Kaiser, J.P. Hofmann, Stability and decomposition pathways of the NiOOH OER active phase of NiO_x electrocatalysts at open circuit potential traced by ex situ and in situ spectroscopies, Catal. Sci. Technol. 13 (16) (2023) 4693–4700.

[44] M. Dekermenjian, A.P. Ruediger, A. Merlen, Raman spectroscopy investigation of magnesium oxide nanoparticles, RSC Adv. 13 (38) (2023) 26683–26689.

[45] G.C. Vásquez, D. Maestre, A. Cremades, J. Piqueras, Assessment of the Cr doping and size effects on the Raman-active modes of rutile TiO_2 by UV/Visible polarized Raman spectroscopy, J. Raman Spectrosc. 48 (6) (2017) 847–854.

[46] J. Klein, L. Kampermann, B. Mockenhaupt, M. Behrens, J. Strunk, G. Bacher, Limitations of the tauc plot method, Adv. Funct. Mater 33 (47) (2023).

[47] C.S. Garoufalis, A. Barnasas, A. Stamatelatos, V. Karoutsos, S. Grammatikopoulos, P. Poulopoulos, S. Baskoutas, A study of quantum confinement effects in ultrathin NiO films performed by experiment and theory, Mater. 11 (6) (2018) 949.

[48] H. Tian, C. Pei, Y. Wu, S. Chen, Z.-J. Zhao, J. Gong, Tunable metal-oxide interaction with balanced NiO/Ni^{2+} sites of $Ni_xMg_{1-x}O$ for ethanol steam reforming, Appl. Catal. B-Environ. 293 (2021) 120178.

[49] C. Freysoldt, B. Grabowski, T. Hickel, J. Neugebauer, G. Kresse, A. Janotti, C.G. Van de Walle, First-principles calculations for point defects in solids, Rev. Modern Phys. 86 (1) (2014) 253–305.

[50] C.G. Van de Walle, J. Neugebauer, First-principles calculations for defects and impurities: Applications to III-nitrides, J. Appl. Phys. 95 (8) (2004) 3851–3879.

[51] M. Nolan, R. Long, N.J. English, D.A. Mooney, Hybrid density functional theory description of N- and C-doping of NiO, J. Chem. Phys. 134 (22) (2011) 224703.

[52] I. Leonov, S. Biermann, Electronic correlations at paramagnetic (001) and (110) NiO surfaces: Charge-transfer and Mott-Hubbard-type gaps at the surface and subsurface of (110) NiO, Phys. Rev. B 103 (2021) 165108.

[53] X. Xu, H. Zhang, Y. Tong, Y. Sun, X. Fang, J. Xu, X. Wang, Tuning Ni^{3+} quantity of NiO via doping of cations with varied valence states: The key role of Ni^{3+} on the reactivity, Appl. Surf. Sci. 550 (2021) 149316.

[54] G. Tyuliev, M. Sokolova, Temperature dependence of Ni^{3+} quantity in the surface layer of NiO, Appl. Surf. Sci. 52 (4) (1991) 343–349.

[55] F. Pielmeier, F.J. Giessibl, Spin resolution and evidence for superexchange on NiO(001) observed by force microscopy, Phys. Rev. Lett. 110 (2013) 266101.

[56] R. Shanker, R.A. Singh, Analysis of the exchange parameters and magnetic properties of NiO, Phys. Rev. B 7 (1973) 5000–5005.

[57] S. Ramachandran, J. Narayan, J.T. Prater, Magnetic properties of Ni-doped MgO diluted magnetic insulators, Appl. Phys. Lett. 90 (13) (2007) 132511.

[58] N. Zhou, Y. Cheng, B. Huang, X. Liao, Effect of nonmagnetic dopants (Ag, Cu or Mg) on ferromagnetic half-metallic properties of NiO, Phys. Rev. B Condens. Matter 557 (2019) 6–11.

[59] W.L. Roth, Magnetic structures of MnO, FeO, CoO, and NiO, Phys. Rev. 110 (1958) 1333–1341.

[60] S. Park, H.-S. Ahn, C.-K. Lee, H. Kim, H. Jin, H.-S. Lee, S. Seo, J. Yu, S. Han, Interaction and ordering of vacancy defects in NiO, Phys. Rev. B 77 (2008) 134103.

[61] K.O. Egbo, C.P. Liu, C.E. Ekuma, K.M. Yu, Vacancy defects induced changes in the electronic and optical properties of NiO studied by spectroscopic ellipsometry and first-principles calculations, J. Appl. Phys. 128 (13) (2020) 135705.

[62] W.-B. Zhang, N. Yu, W.-Y. Yu, B.-Y. Tang, Stability and magnetism of vacancy in NiO: A GGA+U study, Eur. Phys. J. B. 64 (2) (2008) 153–158.

[63] H.T. Sim, M. Gençaslan, M. Merdan, Synthesis of MgO nanoparticles via the sol-gel method for antibacterial applications, investigation of optical properties and comparison with commercial MgO, Discov. Appl. Sci. 6 (11) (2024) 577.

[64] A. Almontasser, A. Parveen, A. Azam, Synthesis, Characterization and antibacterial activity of Magnesium Oxide (MgO) nanoparticles, IOP Conf. Ser. Mater. Sci. Eng. 577 (1) (2019) 012051.

[65] M.A. Zwijnenburg, The effect of particle size on the optical and electronic properties of magnesium oxide nanoparticles, Phys. Chem. Chem. Phys. 23 (2021) 21579–21590.

[66] S. Iida, T. Ikenoue, M. Miyake, T. Hirato, Growth of rock-salt MgO–NiO–ZnO films: Relationship between lattice constant and composition, J. Alloys Compd. 1020 (2025) 179272.

[67] P.G. Mather, J.C. Read, R.A. Buhrman, Disorder, defects, and band gaps in ultrathin (001) MgO tunnel barrier layers, Phys. Rev. B 73 (2006) 205412.

[68] J. Deng, M. Mortazavi, N.V. Medhekar, J. Zhe Liu, Band engineering of $Ni_{1-x}Mg_xO$ alloys for photocathodes of high efficiency dye-sensitized solar cells, J. Appl. Phys. 112 (12) (2012) 123703.

[69] J.J. Bean, M. Saito, S. Fukami, H. Sato, S. Ikeda, H. Ohno, Y. Ikuhara, K.P. McKenna, Atomic structure and electronic properties of MgO grain boundaries in tunnelling magnetoresistive devices, Sci. Rep. 7 (1) (2017) 45594.